The Astrophysical Journal Letters, 938:L16 (9pp), 2022 October 20 https://doi.org/10.3847/2041-8213/ac959e

Early Results from GLASS-JWST. IV. Spatially Resolved Metallicity in a Low-mass $z \sim 3$ Galaxy with NIRISS*

Xin Wang[1,2,3], Tucker Jones[4], Benedetta Vulcani[5], Tommaso Treu[6], Takahiro Morishita[3], Guido Roberts-Borsani[6], Matthew A. Malkan[6], Alaina Henry[7,8], Gabriel Brammer[9,10], Victoria Strait[9,10], Maruša Bradač[4,11], Kristan Boyett[12,13], Antonello Calabrò[14], Marco Castellano[14], Adriano Fontana[14], Karl Glazebrook[15], Patrick L. Kelly[16], Nicha Leethochawalit[12,13,17], Danilo Marchesini[18], P. Santini[14], M. Trenti[12,13], and Lilan Yang[19]
[1] School of Astronomy and Space Science, University of Chinese Academy of Sciences (UCAS), Beijing 100049, People's Republic of China; xwang@ucas.ac.cn
[2] National Astronomical Observatories, Chinese Academy of Sciences, Beijing 100101, People's Republic of China
[3] Infrared Processing and Analysis Center, Caltech, 1200 E. California Boulevard, Pasadena, CA 91125, USA
[4] Department of Physics and Astronomy, University of California Davis, 1 Shields Avenue, Davis, CA 95616, USA
[5] INAF Osservatorio Astronomico di Padova, vicolo dell'Osservatorio 5, I-35122 Padova, Italy
[6] Department of Physics and Astronomy, University of California, Los Angeles, 430 Portola Plaza, Los Angeles, CA 90095, USA
[7] Space Telescope Science Institute, 3700 San Martin Drive, Baltimore MD 21218, USA
[8] Center for Astrophysical Sciences, Department of Physics and Astronomy, Johns Hopkins University, Baltimore, MD 21218, USA
[9] Cosmic Dawn Center (DAWN), Denmark
[10] Niels Bohr Institute, University of Copenhagen, Jagtvej 128, DK-2200 Copenhagen N, Denmark
[11] University of Ljubljana, Department of Mathematics and Physics, Jadranska ulica 19, SI-1000 Ljubljana, Slovenia
[12] School of Physics, University of Melbourne, Parkville 3010, VIC, Australia
[13] ARC Centre of Excellence for All Sky Astrophysics in 3 Dimensions (ASTRO 3D), Australia
[14] INAF Osservatorio Astronomico di Roma, Via Frascati 33, I-00078 Monteporzio Catone, Rome, Italy
[15] Centre for Astrophysics and Supercomputing, Swinburne University of Technology, PO Box 218, Hawthorn, VIC 3122, Australia
[16] School of Physics and Astronomy, University of Minnesota, 116 Church Street SE, Minneapolis, MN 55455, USA
[17] National Astronomical Research Institute of Thailand (NARIT), Mae Rim, Chiang Mai, 50180, Thailand
[18] Department of Physics and Astronomy, Tufts University, 574 Boston Avenue, Medford, MA 02155, USA
[19] Kavli Institute for the Physics and Mathematics of the Universe, The University of Tokyo, Kashiwa, 277-8583, Japan
Received 2022 July 26; revised 2022 September 17; accepted 2022 September 28; published 2022 October 18

Abstract

We report the first gas-phase metallicity map of a distant galaxy measured with the James Webb Space Telescope (JWST). We use the NIRISS slitless spectroscopy acquired by the GLASS Early Release Science program to spatially resolve the rest-frame optical nebular emission lines in a gravitationally lensed galaxy at $z = 3.06$ behind the A2744 galaxy cluster. This galaxy (dubbed GLASS-Zgrad1) has stellar mass $\sim 10^{8.6} M_{\odot}$, instantaneous star formation rate $\sim 8.6\ M_{\odot}\ \mathrm{yr}^{-1}$ (both corrected for lensing magnification), and global metallicity one-fourth solar. From its emission-line maps ([O III], Hβ, Hγ, [Ne III], and [O II]), we derive its spatial distribution of gas-phase metallicity using a well-established forward-modeling Bayesian inference method. The exquisite resolution and sensitivity of JWST/NIRISS, combined with lensing magnification, enable us to resolve this $z \sim 3$ dwarf galaxy in $\gtrsim$50 resolution elements with sufficient signal, an analysis hitherto not possible. We find that the radial metallicity gradient of GLASS-Zgrad1 is strongly inverted (i.e., positive): $\Delta \log(\mathrm{O/H})/\Delta r = 0.165 \pm 0.023$ dex kpc^{-1}. This measurement is robust at $\gtrsim 4-\sigma$ confidence level against known systematics. This positive gradient may be due to tidal torques induced by a massive nearby ($\sim$15 kpc projected) galaxy, which can cause inflows of metal-poor gas into the central regions of GLASS-Zgrad1. These first results showcase the power of JWST wide-field slitless spectroscopic modes to resolve the mass assembly and chemical enrichment of low-mass galaxies in and beyond the peak epoch of cosmic star formation ($z \gtrsim 2$). Reaching masses $\lesssim 10^9\ M_{\odot}$ at these redshifts is especially valuable to constrain the effects of galactic feedback and environment and is possible only with JWST's new capabilities.

Unified Astronomy Thesaurus concepts: Galaxy abundances (574); Galaxy evolution (594); Galaxy formation (595); High-redshift galaxies (734); Strong gravitational lensing (1643)

1. Introduction

A central challenge in galaxy evolution is to understand how galaxies assemble their baryonic mass and cycle their gas and heavy elements in and around themselves. Deep imaging and spectroscopic surveys with the Hubble Space Telescope (HST), the Sloan Digital Sky Survey (SDSS), and other facilities have provided a census of the cosmic star formation rate (SFR) and hence metal enrichment history, which peak at $1 \lesssim z \lesssim 3$ (the "cosmic noon" epoch; e.g., Madau & Dickinson 2014). Dedicated observational campaigns have established tight correlations among various physical properties of star-forming galaxies at this epoch, e.g., stellar mass (M_*), SFR, gas-phase metallicity, size, morphology, kinematics, and dust and gas content (see recent reviews by Kewley et al. 2019; Maiolino & Mannucci 2019). These integrated scaling relations are largely reproduced by theoretical semianalytic models and simulations

* Based on observations acquired by the JWST under the ERS program ID 1324 (PI T. Treu).

that incorporate accretion and merging, star formation, and feedback in the form of gaseous outflows powered by star formation and supermassive black hole accretion (e.g., Somerville and Davé 2015). However, key properties of galactic outflows such as their mass-loss rates and recycling timescales, have proven extremely challenging to discern, especially at intermediate and high redshifts. A variety of assumptions and "subgrid" physical models are able to reproduce global galaxy scaling relations. Hence, additional observational constraints are needed to better understand how feedback redistributes baryons within and around galaxies.

Gas-phase metallicity gradients are sensitive probes of the complex gas flows driven by galactic feedback and tidal interactions. The value of gas metallicity maps as a diagnostic of galaxy formation has been demonstrated by numerous integral field spectroscopy (IFS) surveys at $z = 0$ (e.g., Sanchez et al. 2014; Belfiore et al. 2017; Poetrodjojo et al. 2018; Franchetto et al. 2021). Theoretical models and simulations make differing predictions for metallicity gradient evolution, depending on the strength of feedback and the outflow properties at high redshifts (Gibson et al. 2013). Predictions diverge the most at low stellar masses ($M_* \lesssim 10^9 M_\odot$), especially at $z > 2$ (Gibson et al. 2013; Mott et al. 2013; Molla et al. 2019; Hemler et al. 2021). This is a key regime where feedback may be important for dynamical evolution and is even a candidate to resolve the longstanding "cusp-core" problem (and related challenges to the cold dark matter paradigm; e.g., Bullock & Boylan-Kolchin 2016). However, observations are challenging due to the small angular sizes of high-z galaxies, and ground-based adaptive optics studies have yielded limited samples (e.g., Jones et al. 2013; Yuan et al. 2013; Leethochawalit et al. 2016; Curti et al. 2020. Meanwhile, HST grism surveys have made substantial progress in charting resolved chemical enrichment at high redshifts (Jones et al. 2015; Wang et al. 2017, 2020; Simons et al. 2021; Li et al. 2022). Combining WFC3 grism spectroscopy with gravitational lensing magnification, Wang et al. (2020) assembled a large sample of galaxies with sub-kpc (subkiloparsec) resolution metallicity radial gradients at cosmic noon. While this progress is encouraging, results from HST are limited by wavelength coverage to $z \lesssim 2.3$ and typically probe $M_* \gtrsim 10^9\, M_\odot$.

The Near-infrared Imager and Slitless Spectrograph (NIRISS; Willott et al. 2022) on board the James Webb Space Telescope (JWST) now enables a tremendous leap forward with its superior sensitivity, angular resolution, and longer-wavelength coverage compared to HST/WFC3. This allows resolved metallicity studies probing higher redshifts and lower-mass galaxies, which are a powerful discriminant of feedback and outflow models (e.g., Ma et al. 2017; Hemler et al. 2021). This Letter presents the first study of gas-phase metallicity maps at $z > 3$, a regime not yet explored observationally, based on the NIRISS data acquired by the Early Release Science (ERS) program GLASS-JWST (ID ERS-1324;[20] Treu et al. 2022). These observations also take advantage of the gravitational lensing magnification by the galaxy cluster A2744 to study background high-z sources in high definition.

This Letter is structured as follows. We briefly describe the observations in Section 2. In Section 3 we describe the extraction of emission-line maps and subsequent measurements of gas-phase metallicity (both the global value and spatial map). We discuss the results in Section 4 and summarize the main conclusions in Section 5. We adopt a standard cosmology with $\Omega_m = 0.3$, $\Omega_\Lambda = 0.7$, and $H_0 = 70$ kms^{-1}Mpc^{-1}, and a Chabrier (2003) initial mass function (IMF).

2. Observations

In this Letter, we use JWST/NIRISS data from GLASS-ERS, whose observing strategy is described by Treu et al. (2022), and data reduction in Paper I (Roberts-Borsani et al. 2022). In brief, the A2744 cluster core was observed for ∼15 hr with NIRISS wide-field slitless spectroscopy and direct imaging in three filters (F115W, F150W, and F200W). This provides low-resolution $R \sim 150$ spectra of all objects in the field of view with continuous wavelength coverage from $\lambda \in [1.0, 2.2]$ μm (rest-frame [0.24, 0.54] μm at $z = 3.06$). This includes the strong rest-frame optical emission lines [Mg II], [O II], [Ne III], Hγ, Hβ, and [O III]. Spectra are taken at two orthogonal dispersion angles (using the GR150C and GR150R grism elements), which helps to minimize the effects of contamination by overlapping spectral traces.

3. Data Analysis

Here we focus on the NIRISS observations of one galaxy (GLASS-Zgrad1) at $z = 3.06$, whose measured properties are given in Table 1. GLASS-Zgrad1 has a highly secure grism redshift determination given by GRIZLI, with $(\Delta z)_{\rm posterior}/(1 + z_{\rm peak}) = 1.7 \times 10^{-4}$, ascribed to its extremely strong rest-frame optical emission lines. Its data benefit from low contamination from neighboring sources, so its spectrum is suitable for measuring emission-line maps. The synergy between JWST's resolving power and its lensing magnification (estimated to be ∼3, Johnson et al. 2014; Wang et al. 2015; Bergamini et al. 2022) reveals its detailed physical properties on scales as small as ∼200 pc. These characteristics make our target a textbook case to showcase the capabilities of JWST in spatially resolving the properties of high-z galaxies. The upper-left panel of Figure 1 shows its color composite image, made by combining the three NIRISS filters (F115W, F150W and F200W). The galaxy shows a smooth light profile, with no clear signs of clumpy structures. The location of GLASS-Zgrad1 on the mass–excitation diagram (Juneau et al. 2014; Coil et al. 2015) indicates negligible emission-line contamination from an active galactic nucleus (AGN), such that we can apply standard gas-phase metallicity diagnostics for H II regions.

While GLASS-Zgrad1 itself shows no clear signs of interaction, it is located only ∼15 kpc in projection from a ∼100× more massive galaxy ($M_* \approx 10^{10.6}\, M_\odot$) at a consistent redshift (Sun et al. 2022; Wu et al. 2022). This massive companion shows a potentially spiral structure that may be induced by interaction with GLASS-Zgrad1 (Wu et al. 2022). Such interaction may affect the metallicity gradient via torques on the gas; we discuss this possibility in Section 4.

3.1. Emission-line Map and Metallicity Measurements

We rely on the latest version the Grism Redshift & Line software (GRIZLI;[21] Brammer & Matharu 2021) to extract and

[20] https://www.stsci.edu/jwst/science-execution/approved-programs/dd-ers/program-1324

[21] https://github.com/gbrammer/grizli

Table 1
Physical Properties of Galaxy GLASS-Zgrad1

Galaxy	GLASS-Zgrad1
R.A. (deg)	3.585943
Decl. (deg)	−30.382102
$z_{\rm spec}$	3.06
μ	$3.00^{+0.03}_{-0.03}$
Observed Emission-line Fluxes	
$f_{[\rm O\ III]}$ [10^{-19}ergs^{-1}cm^{-2}]	913.77 ± 9.65
$f_{\rm H\beta}$ [10^{-19}ergs^{-1}cm^{-2}]	161.68 ± 8.89
$f_{\rm H\gamma}$ [10^{-19}ergs^{-1}cm^{-2}]	40.71 ± 12.73
$f_{[\rm Ne\ III]}$ [10^{-19}ergs^{-1}cm^{-2}]	101.65 ± 14.76
$f_{[\rm O\ II]}$ [10^{-19}ergs^{-1}cm^{-2}]	207.43 ± 9.65
Rest-frame Equivalent Widths	
EW$_{[\rm O\ III]}$ [Å]	749.37 ± 25.23
EW$_{\rm H\beta}$ [Å]	156.92 ± 10.18
EW$_{\rm H\gamma}$ [Å]	31.66 ± 9.39
EW$_{[\rm Ne\ III]}$ [Å]	47.80 ± 6.51
EW$_{[\rm O\ II]}$ [Å]	130.52 ± 6.70
Nebular Emission Diagnostics	
$12 + \log(\rm O/H)_{global}$	$8.11^{+0.07}_{-0.06}$
$\Delta \log(\rm O/H)/\Delta r$ [dex kpc^{-1}]	0.165 ± 0.023
SFR$^{\rm N}$ [$M_\odot$ yr^{-1}]	$8.64^{+6.35}_{-2.48}$
log(sSFR$^{\rm N}$/[yr^{-1}])	$-7.68^{+0.34}_{-0.22}$
$A_V^{\rm N}$	$0.54^{+0.63}_{-0.39}$
Broadband Photometry SED Fitting	
$\log(M_*/M_\odot)$	$8.62^{+0.07}_{-0.10}$
SFR$^{\rm S}$ [$M_\odot$ yr^{-1}]	$4.28^{+0.43}_{-0.44}$
log(sSFR$^{\rm S}$/[yr^{-1}])	$-7.97^{+0.07}_{-0.10}$
$A_V^{\rm S}$	$0.60^{+0.03}_{-0.04}$

Note. The values of M_* and SFR have been corrected for lensing magnification.

model the grism spectra, following the procedure described in Paper I. GRIZLI provides contamination-subtracted 1D and 2D grism spectra, along with the best-fit spectroscopic redshifts, as shown in Figure 1 (also see Appendix A of Wang et al. 2019 for the full descriptions of the redshift fitting procedure employed by GRIZLI). We follow the procedures described by Wang et al. (2020) to extract uncontaminated line maps from the 2D grism spectra, also shown in Figure 1. The maps shown here are encompassed by the boundary of the GRIZLI segmentation map (for details, see Roberts-Borsani et al. 2022) defined using conventional source detection parameters largely following the 3D-HST survey (Brammer et al. 2012; Momcheva et al. 2016). We restrict our analysis to this region, where the stellar continuum is detected at high significance. We additionally use the spatially integrated line fluxes measured by GRIZLI to estimate global physical properties as presented in Table 1. When drizzling the 2D grism spectra and emission-line maps, we adopt a plate scale of 30 mas to Nyquist-sample the FWHM of the JWST point-spread function at these wavelengths.

We jointly constrain the ionized gas metallicity ($12 + \log(\rm O/H)$), nebular dust extinction ($A_v^{\rm N}$), and dereddened Hβ line flux ($f_{\rm H\beta}$) using our forward-modeling Bayesian inference method, largely described in Wang et al. (2017, 2019, 2020, 2022). The likelihood function is defined as

$$\mathrm{L} \propto \exp\left(-\frac{1}{2}\cdot\sum_i \frac{(f_{\mathrm{EL}_i} - R_i\cdot f_{\mathrm{H}\beta})^2}{(\sigma_{\mathrm{EL}_i})^2 + (f_{\mathrm{H}\beta})^2\cdot(\sigma_{R_i})^2}\right). \quad (1)$$

where f_{EL_i} and σ_{EL_i} represent the dereddened emission-line (e.g., [O II], Hγ, Hβ, [O III]) flux and its uncertainty (measured from the flux-calibrated error array; see Roberts-Borsani et al. 2022), corrected using the Calzetti et al. (2000) dust extinction law with $A_v^{\rm N}$ as a free parameter. $R_i = \frac{f_{\mathrm{EL}_i}}{f_{\mathrm{H}\beta}}$ is the expected flux ratio of each line with respect to Hβ, based on the adopted metallicity calibrations and intrinsic Balmer decrements, while σ_{R_i} is the intrinsic scatter in R_i. To compute metallicity, we adopt the purely empirical strong line diagnostics prescribed by Bian et al. (2018), calibrated against a sample of local analogs of high-z galaxies according to their location on the BPT (Baldwin et al. 1981) diagram. We note that the dust extinction $A_v^{\rm N}$ is constrained by the metallicity diagnostics in addition to H Balmer line ratios, as described in our earlier work. For example, the characteristic locus of $\rm R_{23}$ versus $\rm O_{32}$ (see, e.g., Shapley et al. 2015) and the intrinsic [O III]/[Ne III] line ratios (Jones et al. 2015) provide constraints on $A_v^{\rm N}$ along with traditional diagnostics such as Hβ/Hγ. The effect of uncertainty in $A_v^{\rm N}$ is included in our metallicity uncertainties. To estimate the instantaneous star formation rate (SFR$^{\rm N}$), we use the Balmer line luminosity assuming the Kennicutt (1998) calibration scaled to the Chabrier (2003) IMF, i.e., $\mathrm{SFR^N} = 1.6\times10^{-42}\frac{L(\mathrm{H}\beta)}{[\mathrm{erg\ s^{-1}}]}$ [$M_\odot$ yr^{-1}].

The forward-modeling Bayesian inference described above is first performed on the integrated emission-line fluxes to yield global values of $12 + \log(\rm O/H)$, $A_v^{\rm N}$, and SFR$^{\rm N}$ (with results listed in Table 1). We then utilize Voronoi tessellation (Cappellari & Copin 2003; Diehl & Statler 2006) as in Wang et al. (2019, 2020) to construct spatial bins with nearly uniform signal-to-noise ratios (S/Ns) of [O III], the strongest emission line available. We apply the Bayesian inference with line fluxes in each Voronoi bin, yielding maps of metallicity and other properties at sub-kpc resolution. Overall, we are able to resolve this $z\sim3$ dwarf galaxy with $\gtrsim$50 resolution elements at an S/N threshold of 10 in [O III].

As this work relies on emission lines spanning multiple spectroscopic filters, we have examined the relative flux calibration accuracy as a potential source of error. Comparing the spectra with both broadband photometric colors and best-fit spectral templates, we estimate that the relative calibration is accurate to within $\lesssim$10% near the center of each filter (F115W, F150W, and F200W). This applies to the strong lines of [O II], [Ne III], Hβ, and [O III] in our $z = 3.06$ target. Calibration uncertainty for [Ne III]/[O II] and [O III]/Hβ appears to be negligible. However, fluxes near band edges appear to be underestimated in some cases, possibly due to the slight misalignment of the expected and actual spectral trace positions. This potentially affects the Hγ line such that its true flux may be ∼20% larger than we report here. We note that the systematic error of this magnitude is smaller than the statistical uncertainty for spatial Voronoi bins (where line ratio uncertainties are $\gtrsim$10% and Hγ is undetected). Any relative calibration error between the F150W and F200W spectra would appear similar to a change in A_v; in this case, our methodology would produce a bias in A_v but not in $12 + \log(\rm O/H)$.

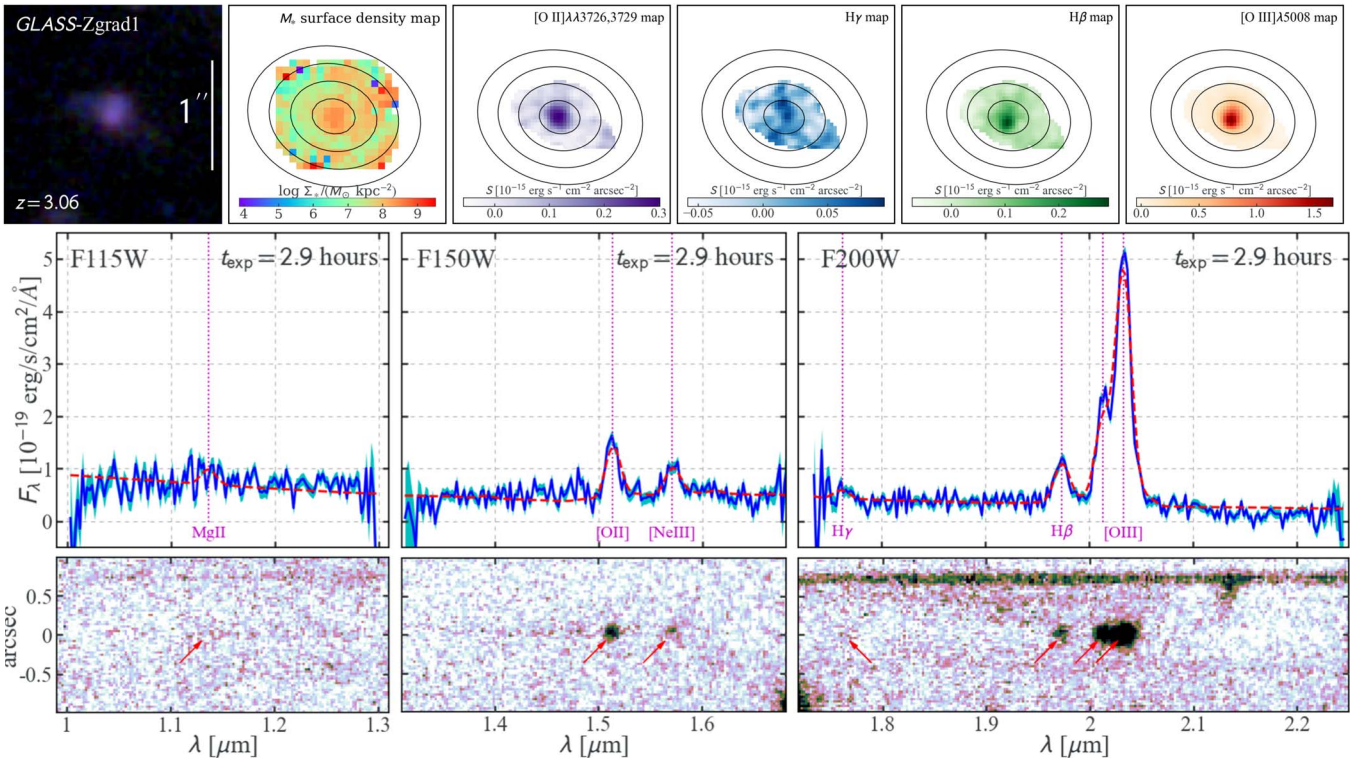

Figure 1. Galaxy GLASS-Zgrad1, a $z \sim 3$ star-forming dwarf galaxy ($M_* \simeq 10^{8.6} M_\odot$) with a strongly inverted metallicity radial gradient presented in this work: the first metallicity map obtained with the JWST and the first-ever such measurement secured by sufficient spatial resolution ($\lesssim$kpc) at $z \geqslant 3$. Top, from left to right: the color composite stamp (made using the three-band JWST/NIRISS pre-imaging on a 30 mas plate scale), stellar surface density (Σ_*) map (derived from the pixel-by-pixel SED fitting), and surface-brightness maps of emission lines ([O II], Hγ, Hβ and [O III]), measured from the NIRISS slitless spectroscopy acquired by GLASS-JWST. The black contours mark the delensed deprojected galactocentric radii with a 1 kpc interval, given by our source-plane morphological reconstruction using the public lens model. The orientation (north up and east to the left) and spatial extent remain unchanged throughout all the 2D maps. Middle: the optimally extracted 1D observed F_λ flux and its 1σ uncertainty, represented by the blue solid lines and cyan shaded bands, respectively, combined from the two orthogonal dispersion directions (GR150C and GR150R). In total, the exposure time per filter combined from both dispersions reaches 2.9 hr. The forward-modeled spectra (source continuum + nebular emission), based on the best-fit intrinsic SED with source morphological broadening taken into account, is shown in the red dashed line. Bottom: the continuum-subtracted 2D grism spectra covered by the three filters (F115W, F150W, and F200W), respectively, showcasing the quality of our GLASS-JWST slitless spectroscopy.

Absolute flux calibration is not needed since our results rely entirely on line ratios. Flux calibration errors therefore may bias the derived A_v but should not substantially affect the spatial trends in metallicity. While a more detailed examination is beyond the scope of this work, for now, we caution that modest NIRISS flux calibration uncertainties may exist and that wavelengths near the bandpass edges should be treated carefully. We anticipate that calibrations will improve over time, as the calibration plan is executed during Cycle 1.

3.2. SED Fitting and Stellar-mass Map

There has been a wealth of deep multiwavelength imaging in broad bands covering 0.2–5 μm wavelengths in the field of A2744. We rely on the photometric catalog compiled by the ASTRODEEP project (Merlin et al. 2016), which performs aperture-matched and blending-corrected photometry of the *HFF* seven-band, Hawk-I Ks, and Spitzer IRAC images (Brammer et al. 2016; Lotz et al. 2017). We use the BAGPIPES software (Carnall et al. 2018) to fit the BC03 models (Bruzual & Charlot 2003) of galaxy spectral energy distributions (SEDs) to the ASTRODEEP photometry. BAGPIPES is capable of adding the nebular emission component into galaxy spectra, so the emission-line fluxes are taken into account in the fit simultaneously. Basic assumptions and parameter ranges include the Chabrier (2003) IMF, a stellar metallicity range of $Z/Z_\odot \in (0, 2.5)$, the Calzetti et al. (2000) dust extinction law with A_v^S in the range of (0, 3), and an exponentially declining star formation history with τ in the range of (0.01, 10)Gyr. We fix the spectroscopic redshift of our galaxy to its best-fit grism value ($z = 3.06$), with a conservative uncertainty of $\Delta z/(1+z) \approx 0.003$, following Momcheva et al. (2016). The obtained physical properties are presented in Table 1. The measured stellar mass and SFR^S are $\log(M_*/M_\odot) = 8.62^{+0.07}_{-0.10}$ and SFR$^S = 4.28^{+0.43}_{-0.44}$, respectively, indicating that our galaxy lies 0.14 dex above the star-forming main sequence (Speagle et al. 2014). We also note that our derived values of the dust reddening for the nebular and stellar component are consistent with $E(B-V)_{\rm stars} \sim E(B-V)_{\rm gas}$ (Reddy et al. 2015).

Broadband image morphology is not necessarily a good tracer of the underlying stellar-mass distribution in star-forming galaxies (e.g., Wuyts et al. 2012). We, therefore, construct stellar-mass maps using spatially resolved SED fitting. We use the same method as Wang et al. (2020), applied to Hubble Frontier Field imaging (Lotz et al. 2017). The F606W, F814W, F105W, F125W, F140W, and F160W HST images are used for this analysis. F435W is not used as it corresponds to the Lyα forest region at $z = 3.06$. Images from each filter are aligned and convolved to a common angular resolution of 0.″22 FWHM, ensuring good sensitivity at low surface brightness reaching beyond the effective radius. The photometry in each 0.″06 square pixel is then fit using FAST (Kriek et al. 2009)

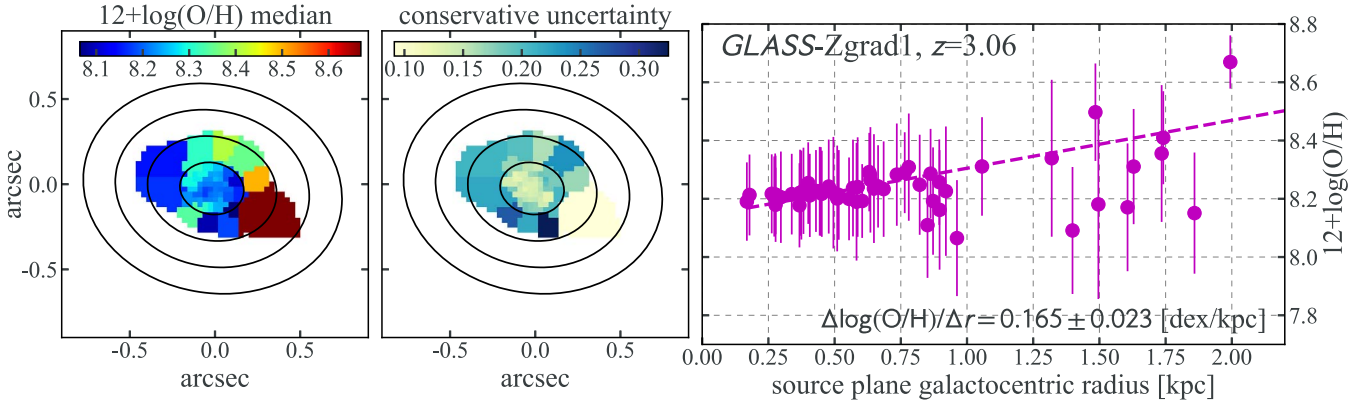

Figure 2. The metallicity spatial maps and radial gradient of GLASS-Zgrad1 at $z \sim 3$. In the left and central panels, we adopt the weighted Voronoi tessellation method (Cappellari & Copin 2003; Diehl & Statler 2006) to divide the galaxy surface into spatial bins with a uniform S/N of 10 on [O III]. The black contours represent the delensed, deprojected galactocentric radii with 1 kpc intervals from our source-plane morphological reconstruction. In the right panel, we show the radial gradient of the metallicity inferences in all individual Voronoi cells, with a slope of $\Delta \log(\mathrm{O/H})/\Delta r = 0.165 \pm 0.023$ [dex kpc^{-1}] represented by the magenta dashed line.

with an exponentially declining star formation history, Chabrier (2003) IMF, and Bruzual & Charlot (2003) stellar population synthesis models (for full details, see Wang et al. 2020). The resulting stellar-mass map is shown in Figure 1. We fit the stellar-mass map with a 2D elliptical Gaussian in order to determine the galactocentric radius at each point (Jones et al. 2015). The stellar-mass surface density is indeed smoother than the luminosity distribution, and we consider morphological parameters based on this mass map to be more reliable.

Future JWST photometry with NIRCam, especially in filters relatively unaffected by strong nebular emission, will enable improved SED-fitting results via spatially resolved photometry at longer wavelengths. Our spatial SED fitting is currently based on HST photometry sampling only $\lesssim$4100 Å in the rest frame. NIRISS F200W imaging would extend the wavelength coverage, but it contains strong emission lines that account for $\sim$55% of the total broadband flux based on the Hβ and [O III] equivalent widths. While this can be corrected using the emission-line maps (Figure 1), the effect of including this additional photometry is small and comparable to the uncertainty. We therefore do not use it for this initial study.

3.3. Source-plane Morphology

We perform a source-plane reconstruction of GLASS-Zgrad1 to recover its intrinsic morphology based on a public lens models (Johnson et al. 2014; Wang et al. 2015; Bergamini et al. 2022). Each pixel in the image-plane stellar-mass map is ray-traced back to its source-plane position based on the deflection fields from the macroscopic cluster lens model. We then fit a 2D Gaussian profile to the galaxy's intrinsic stellar-mass spatial map to pinpoint its axis ratio, orientation, and inclination, so that we obtain the intrinsic source morphology (corrected for lensing distortion). The centroid of this 2D fit is adopted as the galaxy center ($r = 0$). As a result, we establish the delensed deprojected galactocentric distance scale for each Voronoi bin, as displayed by the black contours in Figures 1 and 2.

4. The First Metallicity Map from JWST/NIRISS Wide-field Slitless Spectroscopy

Here we present the main results of our analysis. The top panels of Figure 1 show the maps of the most prominent emission lines of GLASS-Zgrad1: [O II], Hγ, Hβ, and [O III]. Its optimally extracted 1D spectrum, covered by all three grism filters (F115W, F150W, and F200W) combined from both dispersion elements (GR150C and GR150R), is shown in the central row, while the continuum-subtracted 2D grism spectrum is shown in the bottom row. All nebular emission features used in this work are clearly seen. This 1D/2D spectrum showcases the quality of our NIRISS spatially resolved spectroscopy of high-z emission-line galaxies.

The emission-line maps unveil how most of the emission is concentrated in the galaxy core, sharply decreasing at radii $>$1 kpc. In the outskirts, the emission looks quite smooth, especially for [O III]. The only exception is Hγ, which appears patchy due to the lower S/N of this line.

Figure 2 shows the 2D metallicity map of GLASS-Zgrad1. We note that variations in the derived metallicity result directly from the intrinsic emission-line flux ratios via Equation (1) (e.g., as shown for the R_{23} and O_{32} indices for two examples in Figure 2 of Wang et al. 2019). Clearly, the galaxy outskirts on average display highly elevated metallicities, i.e., more metal-enriched by $\sim$0.2 dex than the center. To quantify the radial gradient, we conduct a linear regression using a simple least-squares method, with the functional form $12 + \log(\mathrm{O/H}) = \theta_1 r + \theta_0$. Here, θ_1 and θ_0 are the radial gradient and the intercept, respectively, and r is the source-plane galactocentric radius in kiloparsec. We obtain the best-fit and 1σ uncertainty results as $\theta_1 \equiv \Delta \log(\mathrm{O/H})/\Delta r = 0.165 \pm 0.023$ [dex kpc^{-1}] and $\theta_0 = 8.140 \pm 0.019$. The central metallicity is roughly one-third of the solar value (adopting solar $12 + \log(\mathrm{O/H}) = 8.69$; Asplund et al. 2009) with a significant positive radial gradient. The positive metallicity gradient in GLASS-Zgrad1 is even steeper than those measured by Wang et al. (2019) for two similarly low-mass $z \sim 2$ galaxies, which also show extremely high emission-line equivalent widths and which have gradients of $\sim$0.1 dex/kpc.

We performed several tests to verify that the positive gradient slope is robust against potential systematic errors. First, we have binned the data in radial annuli to obtain a gradient measurement that is independent of the Voronoi tessellation. Using radial bin sizes such that each has S/N $>$ 10 in [O III], we find $\theta_1 = 0.14 \pm 0.03$ dex kpc^{-1}, which is fully consistent with our fiducial result (see also similar tests in

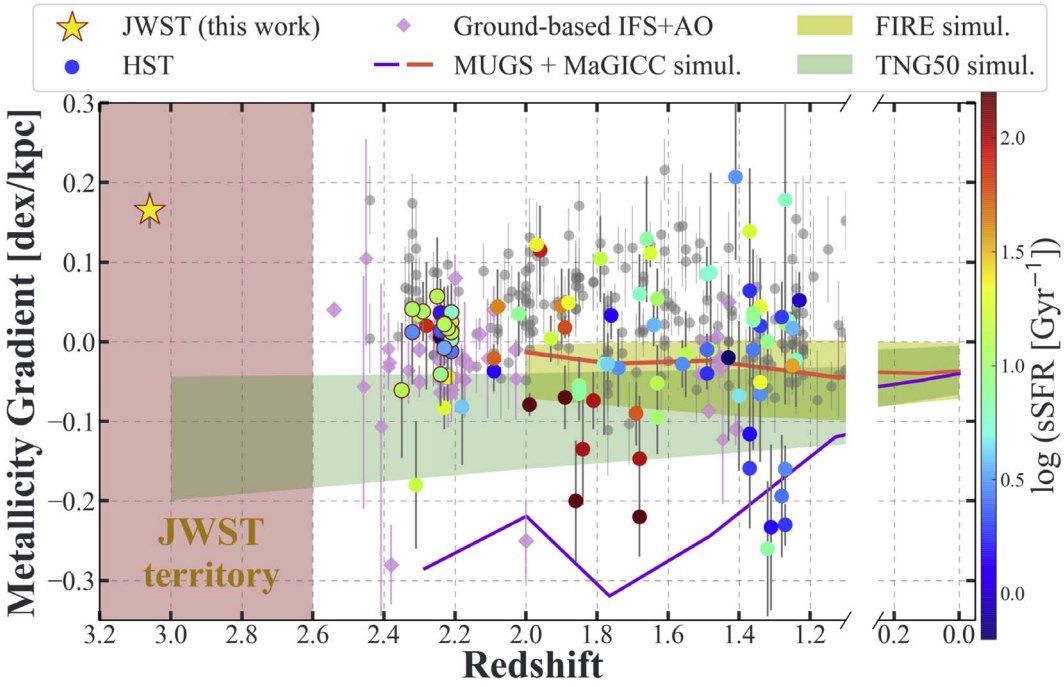

Figure 3. The redshift evolution of sub-kpc resolution metallicity gradients measured from observations and predicted by hydrodynamic simulations. Using the deep NIRISS slitless spectroscopy acquired by GLASS-JWST, we present hitherto the first metallicity gradient measurement with sub-kpc resolution at $z \gtrsim 3$, highlighted by the star color-coded in sSFR. Before this work, all previous observational efforts at similar resolution ($\lesssim$kiloparsec scale) primarily come from ground-based AO-assisted IFS (marked by the magenta diamonds; Swinbank et al. 2012; Jones et al. 2013; Leethochawalit et al. 2016; Schreiber et al. 2018) and space-based slitless spectroscopy with HST/WFC3 (marked by the circles also color-coded in sSFR if such information is publicly available; Jones et al. 2015; Wang et al. 2020; Simons et al. 2021; Li et al. 2022). In particular, we highlight the first measurements of metallicity radial gradients in high-z overdense environments conducted by the MAMMOTH-Grism survey (HST-GO-16276; P.I. Wang; Li et al. 2022) using color-coded circles with maroon edges. In comparison, we show the predictions made by state-of-the-art cosmological hydrodynamic simulations: the 1σ spread of FIRE (Ma et al. 2017) and Illustris-TNG50 (Hemler et al. 2021), as well as two Milky Way analogs with normal and enhanced feedback strengths but otherwise identical numerical setups (corresponding to MUGS and MaGICC, respectively; Gibson et al. 2013). Despite the wide differences among the numerical recipes implemented, these simulations make indistinguishable predictions at $z \lesssim 1$. However, their predictions diverge more significantly at higher redshifts, leaving a potential breakthrough at $z \gtrsim 2.6$, where the JWST spatially resolved spectroscopy can be highly efficient in deriving metallicity gradients and thus test these theoretical predictions.

Wang et al. 2017). Second, we consider whether spurious noise features could bias the results. The largest possible effect is from the highest-metallicity region, which is also at the largest radius ($r \simeq 2$ kpc). Repeating the analysis with this point removed still results in a significant positive gradient $\theta_1 = 0.076 \pm 0.019$ dex kpc^{-1}, albeit smaller than our fiducial result by design. Third, we vary the galaxy center (i.e., $r = 0$ position) by up to $0\farcs1$ and find no significant difference in the results. Finally, to test the statistical significance of the positive slope, we also calculated the Pearson correlation coefficient r_P for metallicity as a function of radius. The result is $r_P = 0.43$ (P-value 0.001), which confirms the significance of the positive slope independent of statistical uncertainty estimates. Taken together, we conclude from these tests that the metallicity gradient slope is indeed positive and on the order of $\gtrsim$0.1 dex kpc^{-1} at $\gtrsim 4\sigma$ significance.

In addition to the steeply rising metallicities indicated by the strong and highly significant ($\geqslant 7\sigma$) inverted radial gradient in GLASS-Zgrad1, there also exist some hints of azimuthal metallicity variations. In particular, the local metallicity shows large variations at radii $r \simeq 1$–2 kpc. This azimuthal structure and deviation from a smooth radial gradient, if further confirmed in numerous high-z galaxies, can shed light upon the timescales for chemical enrichment relative to diffusion and mixing via measurements of the metallicity correlation length scale. This would represent a valuable new constraint for models of galaxy formation at high redshifts (e.g., Metha et al. 2021, 2022).

In Figure 3, we show the redshift evolution of radial metallicity gradients in high-z galaxies secured with sub-kpc spatial resolution. This sub-kpc resolution is crucial in ensuring the results are robust against beam-smearing effects (e.g., Yuan et al. 2013). The vast majority of the galaxies shown here reside in blank fields, with the exceptions of those identified by the MAMMOTH-Grism survey (HST-GO-16276, P.I. Wang, Wang et al. 2022) residing in the core regions of one of the most massive galaxy protoclusters at $z \sim 2.24$ (marked by the maroon edges; Li et al. 2022). The current existing sample in the literature consists of essentially two types of measurements driven by the available infrared spectroscopic instrumentation: ground-based IFS assisted with adaptive optics (AO) (Swinbank et al. 2012; Jones et al. 2013; Leethochawalit et al. 2016; Schreiber et al. 2018) and space-based slitless spectroscopy (Jones et al. 2015; Wang et al. 2020; Simons et al. 2021; Li et al. 2022). The latter method only refers to HST WFC3 spectroscopy before this work. Limited by the wavelength coverage of the WFC3/G141 grism and the H/K-band AO Strehl ratios, there have not yet been any sub-kpc resolution measurements of metallicity maps at $z \geqslant 3$. Using the deep NIRISS slitless spectroscopy acquired by GLASS-JWST, we for the first time secure an inverted gradient in the redshift range of $z \gtrsim 2.6$. This opens up a new key window for an accurate characterization of the chemical profiles of galaxies in and beyond the cosmic noon epoch to constrain the effect of galactic feedback. Notably, we can see from Figure 3 that the theoretical predictions by a number of state-of-the-art

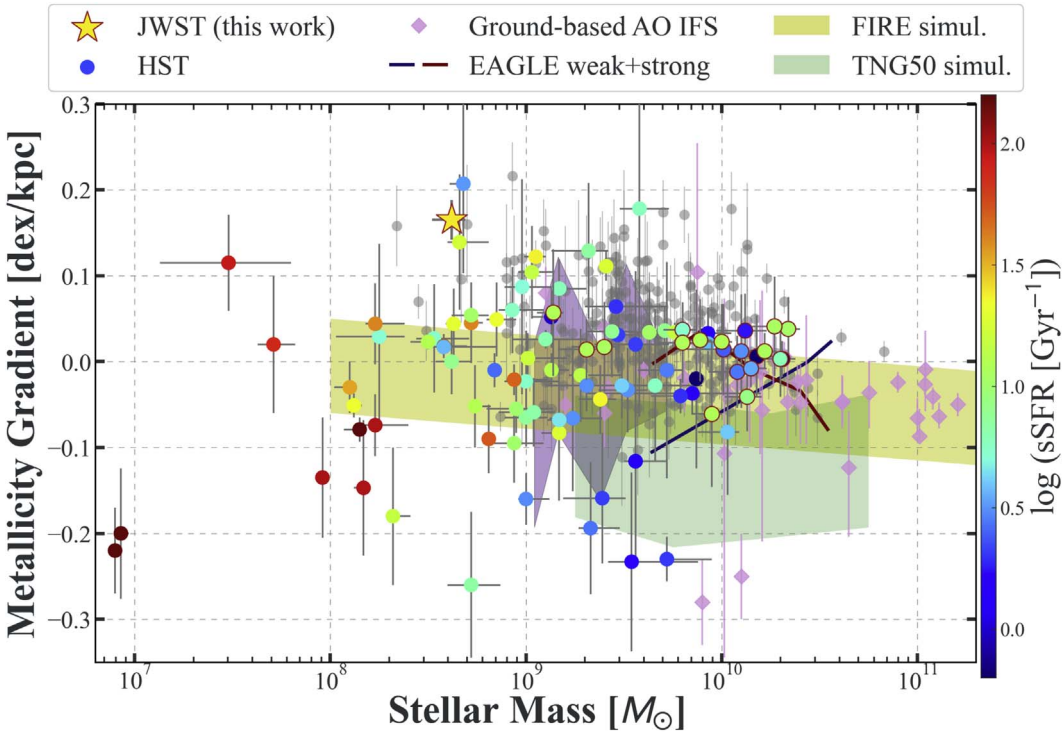

Figure 4. The mass dependence of sub-kpc resolution metallicity gradients measured from observations and predicted by hydrodynamic simulations. All symbols remain the same as in Figure 3, except that the solid lines now represent the predictions by the EAGLE simulations assuming weak or strong feedback prescriptions (Tissera et al. 2019). The $z = 2$ results of the Illustris-TNG50 simulations are shown here. The latest EAGLE results extending to $M_* \sim 10^9 M_\odot$ at $z = 2$ are denoted by the purple shaded regions bracketing the [25th, 75th] percentiles of the simulation predictions, which shows a better agreement with the observed scatters in metallicity gradients (Tissera et al. 2021). As compared to the MAMMOTH-Grism metallicity gradients measured in an overdense environment having a sample median of 0.014 ± 0.022 [dex kpc^{-1}] (Li et al. 2022), GLASS-Zgrad1 shows a much more pronounced inverted gradient, indicating stronger environmental effects. This is consistent with the theoretical prediction that tidal torques, stemming from close gravitational interaction, induce cold gas infalls into the inner disk to invert the metallicity radial gradient (Torrey et al. 2012; Jones et al. 2013, 2015).

cosmological hydrodynamic simulations—FIRE (Ma et al. 2017), Illustris-TNG50 (Hemler et al. 2021), MUGS, and MaGICC (Gibson et al. 2013)—significantly diverge at high redshifts, as a consequence of diverse feedback prescriptions. They also struggle to reproduce the fraction of inverted (positive slope) gradients currently observed.

The existence of a relatively steep positive metallicity gradient in GLASS-Zgrad1 is at first surprising, given the predominantly flat or moderately negative radial gradients in Figure 3. However, GLASS-Zgrad1 has a massive companion that may be gravitationally interacting (Section 3; Wu et al. 2022). Such an interaction can induce torques on the gas, causing metal-poor gas at large radii to lose angular momentum and migrate toward the center of the galaxy. This process can result in flattened or inverted metallicity gradients (e.g., Kewley et al. 2006). Indeed, close gravitational interaction is the primary driver of positive gradients in $z \simeq 0$ galaxies (e.g., Rupke et al. 2010; Torrey et al. 2012). We therefore consider it likely that the gradient in our target is indeed steeply positive and is induced by interaction with the nearby object.

In Figure 4, we show the metallicity gradients of these field galaxies in terms of their M_*. This correlation is highly sensitive to galactic feedback. For instance, the two suites of EAGLE simulations using different feedback prescriptions predict widely dissimilar mass dependence (Tissera et al. 2019). Observationally there is considerable scatter in the metallicity gradient slopes, which the current state-of-the-art numerical hydrodynamic simulations (e.g., Ma et al. 2017; Hemler et al. 2021) struggle to reproduce (but see Tissera et al. 2021).

Recently, there has been growing evidence for the existence of inverted metallicity gradients in distant galaxies (Cresci et al. 2010; Wang et al. 2019; Li et al. 2022). Wang et al. (2019) interpreted this phenomenon as an indication of the metal-enriched gas outflows triggered by central starbursts that disrupt galaxies out of equilibrium (also see Sharda et al. 2021), whereas other groups have suggested centrally directed low-metallicity gas infall as the physical cause (Cresci et al. 2010; Mott et al. 2013). The latter scenario has been adopted to explain the inverted gradients observed in protocluster environments where gas inflows are easily drawn by the underlying large gravitational potentials (Li et al. 2022). Here our analysis confirmed a third scenario where strongly inverted gradients at high redshifts can be caused by the inflow of metal-poor gas into inner disks as a result of close gravitational interactions. Furthermore, as shown in Figures 3 and 4, the magnitude of the positive radial slope measured in GLASS-Zgrad1 is significantly more dramatic than the sample median of 0.014 ± 0.022 [dex kpc^{-1}] measured in the MAMMOTH-Grism galaxies residing in extreme overdensities (Li et al. 2022). This likely suggests that gravitational interactions impose stronger environmental effects on the chemical profiles of high-z galaxies than large-scale overdensities.

5. Conclusions

In this Letter, we present the first spatially resolved analysis of a high-z emission-line galaxy using the wide-field slitless

spectroscopic modes provided by JWST. We first showcase the quality of our NIRISS grism data acquired by the GLASS-JWST-ERS program, presenting the extracted and cleaned 1D/2D grism spectra of a $z \simeq 3$ dwarf galaxy, GLASS-Zgrad1. Via SED fitting to the broadband photometry fully covering its rest-frame UV through optical spectrum, we obtain $\log(M_*/M_\odot) = 8.62^{+0.07}_{-0.10}$ and $\mathrm{SFR}^S = 4.28^{+0.43}_{-0.44}$ [$M_\odot$ yr^{-1}] corrected for lensing magnification ($\mu = 3.00 \pm 0.03$), $\sim$0.14 dex above the star-forming main sequence at $z \sim 3$. From the optimally extracted 1D grism spectrum (in particular the rest-frame optical nebular emission lines: [O III], Hβ, Hγ, and [O II]), we measure its global physical properties to be $12 + \log(\mathrm{O/H})_{\mathrm{global}} = 8.11^{+0.07}_{-0.06}$, $\mathrm{SFR}^{\mathrm{N}} = 8.64^{+6.35}_{-2.48}$ [$M_\odot$ yr^{-1}], and $A_V^{\mathrm{N}} = 0.54^{+0.63}_{-0.39}$, consistent with $E(B-V)_{\mathrm{stars}} \sim E(B-V)_{\mathrm{gas}}$.

Importantly, the new capabilities afforded by JWST/NIRISS (e.g., exquisite sensitivity, resolution, and wavelength coverage, etc.), coupled with gravitational lensing magnification, enable us to spatially resolve GLASS-Zgrad1 into $\gtrsim$50 individual resolution elements with source-plane resolution reaching $\sim$200 pc scales. Using its multiple nebular emission-line maps, we determine its metallicity radial gradient to be highly inverted (positive), i.e., $\Delta \log(\mathrm{O/H})/\Delta r = 0.165 \pm 0.023$ [dex kpc^{-1}]. This is the first-ever metallicity map from JWST spectroscopy, and the first sub-kpc resolution metallicity gradient ever measured at $z \gtrsim 3$. We also verified this positive gradient slope through extensive tests. In particular, by removing the outermost spatial bin at $r \simeq 2$~kpc showing significant metal enhancement, we rederived the gradient slope to be 0.076 ± 0.019 dex kpc^{-1}, vindicating our finding that in \galname the abundance of metals increases with galacto-centric radius.

This strongly inverted metallicity gradient of GLASS-Zgrad1 likely stems from the close gravitational interaction with a nearby object—a dusty galaxy $\sim$100$\times$ more massive than GLASS-Zgrad1 at a projected separation of $\sim$15 kpc. This close encounter results in powerful tidal torques to induce metal-poor gas inflows to the inner regions of GLASS-Zgrad1, inverting its radial metallicity gradient. We thereby confirm a third channel for high-z galaxies showing a strongly inverted metallicity gradient, in addition to cold-mode accretion and metal-enriched gas outflows. Moreover, in light of the more pronounced inverted gradient measured in GLASS-Zgrad1 than any of the MAMMOTH-Grism gradient sources, we deduce that close gravitational interactions are more capable of producing strong environmental effects that modulate the chemical profiles of galaxies than large-scale overdensities (e.g., protocluster cores) at high redshifts. Our subsequent analysis of a larger sample within the GLASS-JWST data set will enable more comprehensive investigations of the true chemical profiles of galaxies at $z \sim 3$ so that we can make a quantitative comparison to simulations and hence cast more meaningful constraints on the effects of mergers, galactic feedback, and environments. This work marks the beginning of a new era for spatially resolved analysis of galaxy chemostructural evolution in and beyond the cosmic noon epoch.

We would like to thank the anonymous referee for careful reading and constructive comments that help improve the clarity of this paper. This work is based on observations made with the NASA/ESA/CSA James Webb Space Telescope. The data were obtained from the Mikulski Archive for Space Telescopes at the Space Telescope Science Institute, which is operated by the Association of Universities for Research in Astronomy, Inc., under NASA contract NAS 5-03127 for JWST. These observations are associated with program JWST-ERS-1324. We acknowledge financial support from NASA through grant JWST-ERS-1324. X.W. is supported by CAS Project for Young Scientists in Basic Research, Grant No. YSBR-062. X.W. thanks Zach Hemler for kindly providing his compilations of gradient measurements from the literature and Patricia Tissera for providing the tabulated results of the latest EAGLE simulations. K.G. acknowledges support from Australian Research Council Laureate Fellowship FL180100060. M.B. acknowledges support from the Slovenian national research agency ARRS through grant N1-0238.

ORCID iDs

Xin Wang https://orcid.org/0000-0002-9373-3865
Tucker Jones https://orcid.org/0000-0001-5860-3419
Benedetta Vulcani https://orcid.org/0000-0003-0980-1499
Tommaso Treu https://orcid.org/0000-0002-8460-0390
Takahiro Morishita https://orcid.org/0000-0002-8512-1404
Guido Roberts-Borsani https://orcid.org/0000-0002-4140-1367
Matthew A. Malkan https://orcid.org/0000-0001-6919-1237
Alaina Henry https://orcid.org/0000-0002-6586-4446
Gabriel Brammer https://orcid.org/0000-0003-2680-005X
Victoria Strait https://orcid.org/0000-0002-6338-7295
Maruša Bradač https://orcid.org/0000-0001-5984-0395
Kristan Boyett https://orcid.org/0000-0003-4109-304X
Antonello Calabrò https://orcid.org/0000-0003-2536-1614
Marco Castellano https://orcid.org/0000-0001-9875-8263
Adriano Fontana https://orcid.org/0000-0003-3820-2823
Karl Glazebrook https://orcid.org/0000-0002-3254-9044
Patrick L. Kelly https://orcid.org/0000-0003-3142-997X
Nicha Leethochawalit https://orcid.org/0000-0003-4570-3159
Danilo Marchesini https://orcid.org/0000-0001-9002-3502
P. Santini https://orcid.org/0000-0002-9334-8705
M. Trenti https://orcid.org/0000-0001-9391-305X
Lilan Yang https://orcid.org/0000-0002-8434-880X

References

Asplund, M., Grevesse, N., Sauval, A. J., & Scott, P. 2009, ARA&A, 47, 481
Baldwin, J. A., Phillips, M. M., & Terlevich, R. 1981, PASP, 93, 5
Belfiore, F., Maiolino, R., Tremonti, C., et al. 2017, MNRAS, 469, 151
Bergamini, P., Acebron, A., Grillo, C., et al. 2022, arXiv:2207.09416
Bian, F., Kewley, L. J., & Dopita, M. A. 2018, ApJ, 859, 175
Brammer, G., & Matharu, J. 2021, gbrammer/grizli: Release 2021, v1.3.2, Zenodo
Brammer, G. B., van Dokkum, P. G., Franx, M., et al. 2012, ApJS, 200, 13
Brammer, G. B., Marchesini, D., Labbe, I., et al. 2016, ApJS, 226, 6
Bruzual, G., & Charlot, S. 2003, MNRAS, 344, 1000
Bullock, J. S., & Boylan-Kolchin, M. 2016, ARA&A, 55, 343
Calzetti, D., Armus, L., Bohlin, R. C., et al. 2000, ApJ, 533, 682
Cappellari, M., & Copin, Y. 2003, MNRAS, 342, 345
Carnall, A. C., McLure, R. J., Dunlop, J. S., & Dave, R. 2018, MNRAS, 480, 4379
Chabrier, G. 2003, PASP, 115, 763
Coil, A. L., Aird, J., Reddy, N., et al. 2015, ApJ, 801, 35
Cresci, G., Mannucci, F., Maiolino, R., et al. 2010, Natur, 467, 811
Curti, M., Maiolino, R., Cirasuolo, M., et al. 2020, MNRAS, 492, 821
Diehl, S., & Statler, T. S. 2006, MNRAS, 368, 497
Franchetto, A., Mingozzi, M., Poggianti, B. M., et al. 2021, ApJ, 923, 28

Gibson, B. K., Pilkington, K., Brook, C. B., Stinson, G. S., & Bailin, J. 2013, A&A, 554, A47
Hemler, Z. S., Torrey, P., Qi, J., et al. 2021, MNRAS, 506, 3024
Johnson, T. L., Sharon, K., Bayliss, M. B., et al. 2014, ApJ, 797, 48
Jones, T., Martin, C., & Cooper, M. C. 2015, ApJ, 813, 126
Jones, T., Ellis, R. S., Richard, J., & Jullo, E. 2013, ApJ, 765, 48
Jones, T., Wang, X., Schmidt, K. B., et al. 2015, AJ, 149, 107
Juneau, S., Bournaud, F., Charlot, S., et al. 2014, ApJ, 788, 88
Kennicutt, R. C. J. 1998, ARA&A, 36, 189
Kewley, L. J., Geller, M. J., & Barton, E. J. 2006, AJ, 131, 2004
Kewley, L. J., Nicholls, D. C., & Sutherland, R. S. 2019, ARA&A, 57, 511
Kriek, M., van Dokkum, P. G., Franx, M., Illingworth, G. D., & Magee, D. K. 2009, ApJ, 705, L71
Leethochawalit, N., Jones, T. A., Ellis, R. S., et al. 2016, ApJ, 820, 84
Li, Z., Wang, X., Cai, Z., et al. 2022, ApJL, 929, L8
Lotz, J. M., Koekemoer, A., Coe, D., et al. 2017, ApJ, 837, 97
Ma, X., Hopkins, P. F., Feldmann, R., et al. 2017, MNRAS, 466, 4780
Madau, P., & Dickinson, M. E. 2014, ARA&A, 52, 415
Maiolino, R., & Mannucci, F. 2019, A&ARv, 27, 3
Merlin, E., Amorín, R., Castellano, M., et al. 2016, A&A, 590, A30
Metha, B., Trenti, M., & Chu, T. 2021, MNRAS, 508, 489
Metha, B., Trenti, M., Chu, T., & Battisti, A. 2022, MNRAS, 514, 4465
Mollá, M., Díaz, A. I, Cavichia, O., et al. 2019, MNRAS, 482, 3071
Momcheva, I. G., Brammer, G. B., van Dokkum, P. G. V., et al. 2016, ApJS, 225, 27
Mott, A., Spitoni, E., & Matteucci, F. 2013, MNRAS, 435, 2918
Poetrodjojo, H. M., Groves, B. A., Kewley, L. J., et al. 2018, MNRAS, 479, 5235
Reddy, N. A., Kriek, M., Shapley, A. E., et al. 2015, ApJ, 806, 259
Roberts-Borsani, G., Morishita, T., Treu, T., et al. 2022, arXiv:2207.11387
Rupke, D. S. N., Kewley, L. J., & Barnes, J. E. 2010, ApJ, 710, L156
Sanchez, S. F., Rosales-Ortega, F., Iglesias-Páramo, J., et al. 2014, A&A, 563, A49
Schreiber, N. M. F., Renzini, A., Mancini, C., et al. 2018, ApJS, 238, 21
Shapley, A. E., Reddy, N. A., Kriek, M., et al. 2015, ApJ, 801, 88
Sharda, P., Krumholz, M. R., Wisnioski, E., et al. 2021, MNRAS, 502, 5935
Simons, R. C., Papovich, C., Momcheva, I., et al. 2021, ApJ, 923, 203
Somerville, R. S., & Davé, R. 2015, ARA&A, 53, 51
Speagle, J. S., Steinhardt, C. L., Capak, P. L., & Silverman, J. D. 2014, ApJS, 214, 15
Sun, F., Egami, E., Fujimoto, S., et al. 2022, ApJ, 932, 77
Swinbank, A. M., Sobral, D., Smail, I., et al. 2012, MNRAS, 426, 935
Tissera, P. B., Rosas-Guevara, Y., Bower, R. G., et al. 2019, MNRAS, 482, 2208
Tissera, P. B., Rosas-Guevara, Y., Sillero, E., et al. 2021, MNRAS, 511, 1667
Torrey, P., Cox, T. J., Kewley, L., & Hernquist, L. 2012, ApJ, 746, 108
Treu, T., Roberts-Borsani, G., Bradac, M., et al. 2022, ApJ, 935, 110
Wang, X., Hoag, A., Huang, K. -H., et al. 2015, ApJ, 811, 29
Wang, X., Jones, T. A., Treu, T., et al. 2017, ApJ, 837, 89
Wang, X., Jones, T. A., Treu, T., et al. 2019, ApJ, 882, 94
Wang, X., Jones, T. A., Treu, T., et al. 2020, ApJ, 900, 183
Wang, X., Li, Z., Cai, Z., et al. 2022, ApJ, 926, 70
Willott, C. J., Doyon, R., Albert, L., et al. 2022, PASP, 134, 025002
Wu, Y., Cai, Z., Sun, F., et al. 2022, arXiv:2208.08473
Wuyts, S., Förster Schreiber, N. M., Genzel, R., et al. 2012, ApJ, 753, 114
Yuan, T., Kewley, L. J., & Rich, J. A. 2013, ApJ, 767, 106